In situ confirmation of permeability development in shearing bubble-bearing melts and implications for volcanic outgassing

Alexandra Roma Larisa Kushnir, Caroline Martel, Rémi Champallier, Laurent Arbaret

In situ confirmation of permeability development in shearing bubble-bearing melts and implications for volcanic outgassing

Alexandra R.L. Kushnir *, Caroline Martel, Rémi Champallier, Laurent Arbaret

Institut des Sciences de la Terre d'Orléans (ISTO), UMR 7327 – CNRS/Université d'Orléans/BRGM, 1A, Rue de la Férollerie, 45071 Orléans Cedex 2, France

ARTICLE INFO

Article history:
Received 5 July 2016
Received in revised form 25 October 2016
Accepted 25 October 2016
Available online xxxx
Editor: T.A. Mather

Keywords:
Mode I fractures
torsion
magma
outgassing
experiments

ABSTRACT

The ferocity of volcanic eruptions – their penchant for either effusive or explosive behaviour – is to a large extent a matter of the ease with which volatiles are able to escape the volcanic system. Of particular importance are the mechanisms by which permeable networks within magma are fabricated and how they permit gas escape, thereby diffusing possibly calamitous explosions. Here, we present a series of experiments that confirms sample-scale fracture propagation and permeability development during shearing viscous flow of initially impermeable, bubble-bearing (<0.20 bubble fraction) magmas under conditions pertinent to volcanic conduits. These samples are deformed in torsion at constant shear strain rates until an applied differential pore fluid pressure across the sample equilibrates, confirming permeability development *in situ*. Permeability develops at moderate to high shear strain rates ($\dot{\gamma} > 2 \times 10^{-4}$ s^{-1}). At moderate shear strain rates (2×10^{-4} s$^{-1} < \dot{\gamma} < 4.5 \times 10^{-4}$ s^{-1}), permeability initiates at high strain ($\gamma > 3$) via en échelon Mode I fractures produced by repeated fracture events. At high shear strain rates ($\dot{\gamma} > 4.5 \times 10^{-4}$ s^{-1}), permeability develops shortly after the onset of inelastic deformation and is, again, established through a series of en échelon Mode I fractures. Critically, strain is not immediately localized on Mode I fractures, making them long-lived and efficient outgassing channels that are ideally oriented for directing volatiles from the central conduit upward and outward toward the conduit rim. Indeed, Mode I fracture arrays may prove necessary for dissipating gas overpressures in the central regions of the magma column, which are considered difficult to outgas. These experiments highlight mechanisms that are likely active along conduit margins and constrain previously postulated processes under truly applicable conditions.

1. Introduction

The ease of gas escape from a volcanic system exerts a fundamental control on eruption style (Eichelberger et al., 1986; Woods and Koyaguchi, 1994). The effusion of silicic magmas occurs when magma is efficiently outgassed, curbing overpressure development and avoiding magma fragmentation, whereas, explosive eruptions and attendant fragmentation occur, in part, when magma is unable to sustain the shear stresses to which it is exposed. Thus, the conditions under which permeability develops within a rising and, therefore, deforming magma column are also conditions under which gas overpressure development and explosive behaviour may be avoided.

Porosity in magmas initially develops from decompression – (Sparks, 1978) and thermally-induced (Lavallée et al., 2015) vesiculation of isolated, pressurized bubbles, which supply the buoyant forces necessary to drive magma upward. Ultimately, gas can only escape through a connected porosity network that eventually leads to the surface. To do this, the isolated bubble structure must be modified and become connected by expansion- (Burgisser and Gardner, 2004) and shear-induced bubble coalescence (Okumura et al., 2008) and/or magma rupture (e.g. Stasiuk et al., 1996). These gases then need to make use of pre-existing permeable networks, like those found in edifice- and dome-forming rocks (e.g. Eichelberger et al., 1986; Woods and Koyaguchi, 1994) or, when these escape routes are insufficient, by magma fragmentation (e.g. Kennedy et al., 2005). This interconnected void space can be created over time (Martel and Iacono-Marziano, 2015), often periodically (Tuffen et al., 2003), and subsequently destroyed (Rust and Cashman, 2004), making permeability in volcanic systems difficult to constrain.

When confronted with exceedingly high strain rates, magma is eventually susceptible to fracture (Webb and Dingwell, 1990b). Shear fractures near conduit edges facilitate gas escape by locally increasing permeability (Gaunt et al., 2014) and are preserved as ash-filled shear and extension fractures (commonly referred to

* Corresponding author.
E-mail address: alexandra.kushnir@gmail.com (A.R.L. Kushnir).

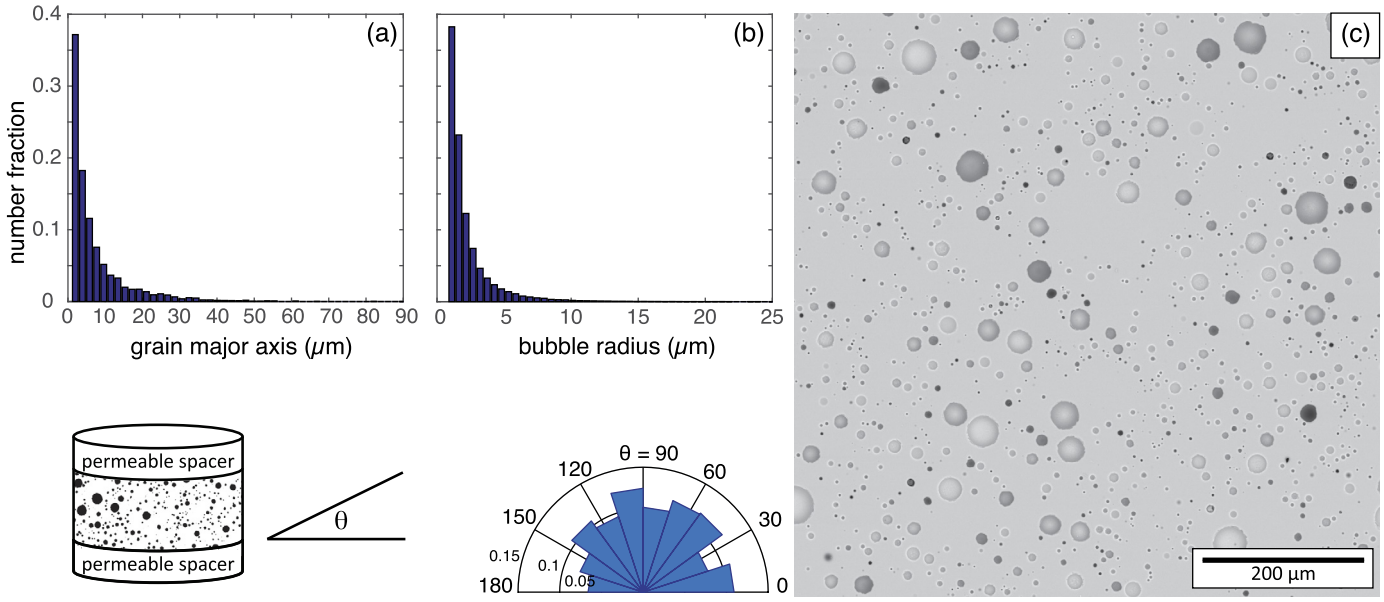

Fig. 1. Starting material. **(a)** 2D grain size distribution for the starting HPG8 powder. We defined the grain size by the length of the longest axis of the powder grains. The powder grain size is <90 μm, with a dominant grain size of 2 μm. **(b)** 2D bubble radius distribution for the synthesized bubble-bearing magma. The polydisperse bubbles have a maximum and peak radius of 25 μm and 2 μm, respectively. **(c)** SEM image of PP506, after synthesis. The rose diagram gives the orientations, θ, of the semi-major axes of the bubbles in the starting material, where θ is angle between the bubble semi-major axis and the shear zone boundary (the permeable spacer interface). Bubble/grain size distributions and orientations were determined by image analysis (using ImageJ) of SEM images. We note that, assuming the argon pore fluid behaves as an ideal gas under the experimental conditions described in the text, the isobaric decompression of the samples led to a 4-fold increase in total porosity and an increase in bubble radius by a factor of 1.6.

as tuffisite veins; e.g. Stasiuk et al., 1996; Tuffen et al., 2003; Castro et al., 2012). These fractures act as efficient transport networks for fluid flow, though repeated fracture events may be necessary to maintain permeability (e.g. Tuffen and Dingwell, 2005; Castro et al., 2012; Shields et al., 2016). Indeed, low-frequency earthquakes at conduit margins suggest that the occurrence of such fracture events is not unusual (e.g. Goto, 1999; Tuffen et al., 2003; Thomas and Neuberg, 2012). Unfortunately, shear-induced deformation along conduit walls may be relatively inefficient at outgassing the conduit centre (e.g. Castro et al., 2012; Gaunt et al., 2014) and strain localization along shear fractures may even limit further outgassing, eventually shutting off the permeable network lining the conduit rim (Okumura et al., 2010).

Several experimental studies have investigated permeability development as magma is deformed in simple shear. Permeability development facilitated by shear-induced bubble coalescence in magmas with moderate to high bubble fractions (>0.20) has been demonstrated experimentally (e.g. Okumura et al., 2008). At low bubble fraction (<0.20), crystal-assisted strain localization can result in bubble coalescence, locally increasing strain rates and inciting cataclastic behaviour that produces Riedel shear geometries (Laumonier et al., 2011). While shear-induced bubble coalescence and outgassing have been inferred in bubble-bearing phonolites containing less than 0.02 bubble fraction (Caricchi et al., 2011), outgassing in two- and three-phase magmas with low bubble fractions (<0.20) appears to be most efficiently facilitated by the development of helical shear fractures (Cordonnier et al., 2012; Shields et al., 2014). Shields et al. (2014) demonstrated that these helical fractures were composed of extension fractures (otherwise termed tensions gashes) oriented approximately perpendicular to the shear direction. Significantly, in the majority of these studies, gas escape was inferred postmortem (that is, post-experiment) by an overall reduction in bubble content (Pistone et al., 2012; Shields et al., 2014) and dissolved volatiles in the melt phase (Shields et al., 2014), making it difficult to identify when and by what mechanisms permeability developed. In particular, sample-scale permeability development in shearing viscous flow via fracture development has not yet been confirmed *in situ*.

The purpose of this study is to begin to experimentally constrain permeability-producing processes previously postulated to be active at conduit margins. We demonstrate the mechanisms by which permeability develops in rhyolitic magmas of relatively low bubble fraction under conditions pertinent to volcanic conduits. We characterize permeability development *in situ* during simple shear of an initially impermeable, haplogranitic, two-phase (bubble and melt) magma as a function of shear strain rate. Further, we associate permeability development with microstructure to identify what mechanisms may influence volcanic behaviour in a natural setting.

2. Methods

Bubble-bearing magma analogues were synthesized and deformed in simple shear using an internally heated, gas-medium (argon) Paterson deformation apparatus equipped with a torsion motor and pore fluid pressure system (Paterson and Olgaard, 2000; Australian Scientific Instruments Pty Ltd; at ISTO, Orléans, France). Each experiment was performed in two steps: i) sample synthesis and ii) sample deformation, detailed below.

2.1. Starting material synthesis

To achieve a homogeneous, reproducible, bubble-bearing magma, we synthesized each sample prior to deformation. The anhydrous silicate melt had an haplogranitic composition (HPG8; prepared by Schott AG, Germany; see Supplementary Material for composition) and was chosen because it is rheologically well-characterized (Hess et al., 2001) and, as the eutectic composition of the quartz–albite–orthoclase system (Holtz et al., 1992), can be deformed at relatively low temperature without crystallisation perturbing its rheology. The HPG8 glass was ground in an agate mechanical grinder and sieved to below 90 μm; this polydisperse powder had a dominant grain length of 2 μm (determined by image analysis, see below for details; Fig. 1A). For each experiment,

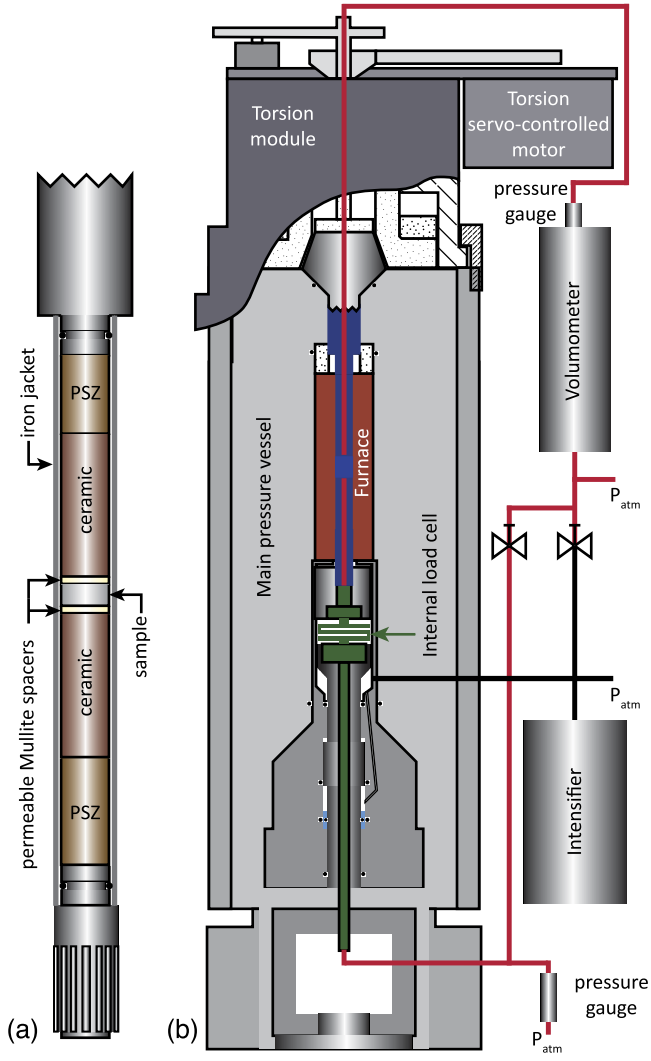

Fig. 2. Sample assembly and Paterson deformation apparatus. **(a)** Sample assembly configuration. **(b)** Schematic of the Paterson deformation apparatus and the pore fluid pressure system, modified from Paterson and Olgaard (2000).

1.5 g of HPG8 powder was placed between two permeable ceramic spacers (Umicore Mullite ceramic; connected porosity, $\phi_c = 0.17$; permeability, $k = 2.7 \times 10^{-16}$ m^2) that were 15 mm in diameter and jacketed in a 0.2 mm thick iron sleeve (Fig. 2A). The sample was placed in the deformation apparatus and pressurized argon gas was introduced into the interstitial space between grains via the pore fluid system (Fig. 2B).

The gas was trapped as bubbles by sintering the powder. To facilitate quick synthesis, we chose to synthesize the magma at $T = 1150\,°C$ using a heating rate of 10 °C/min (Fig. 3A). The sample was located in an isothermal zone (±2 °C) and was monitored using a N-type thermocouple placed 3 mm above the sample. During bubble synthesis, the confining pressure (P_c) and pore fluid pressure (P_f) were both equal to 310 MPa, resulting in an effective pressure ($P_{eff} = P_c - P_f$) equal to 0 MPa (Fig. 3A). This effective pressure ensured that the sample's cylindrical geometry was preserved as the powder sintered.

Given the grain size distribution of the HPG8 powder, we can constrain the characteristic timescale for sintering of droplets of a high viscosity liquid (Wadsworth et al., 2014): $\lambda_s = \frac{R\eta_0}{\Gamma}$, where R is the particle radius, η_0 is the melt viscosity, and Γ is the surface tension between the melt and gas phase. The viscosity of HPG8 at 1150 °C is extrapolated from Hess et al. (2001) and is found to be

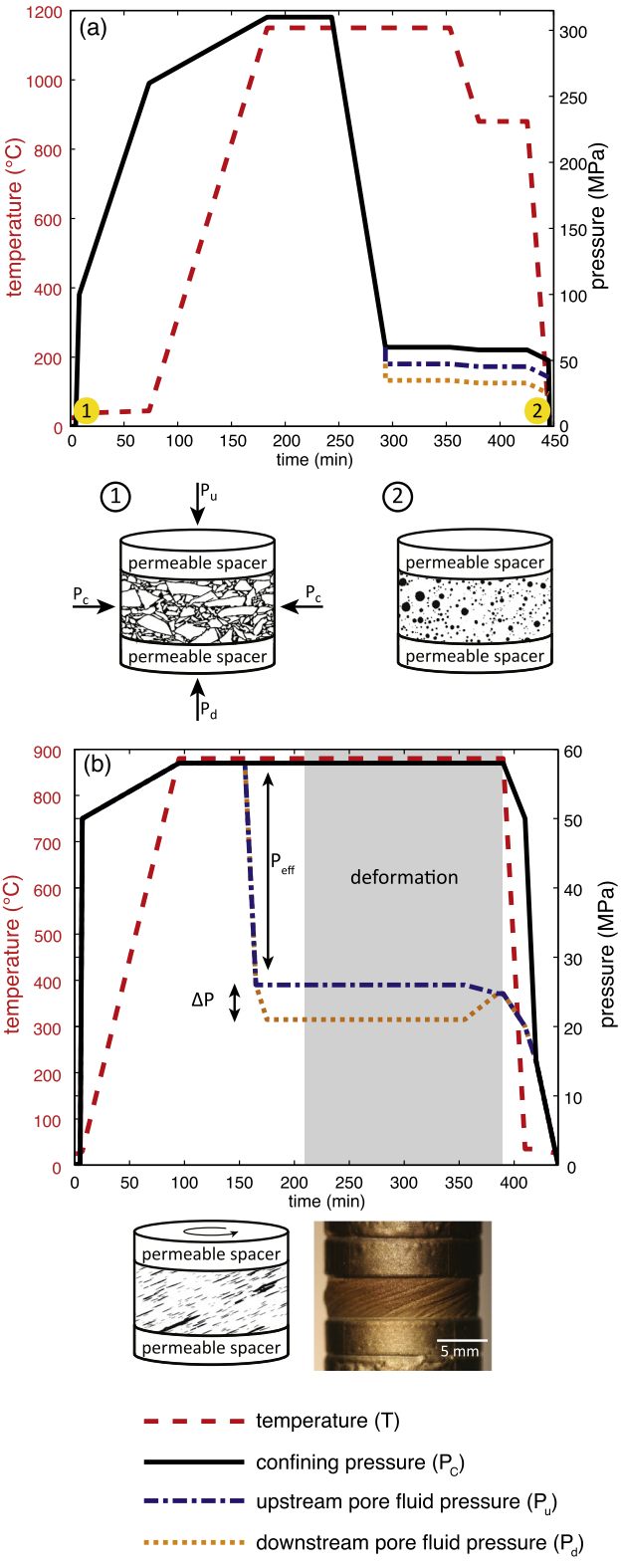

Fig. 3. Schematic representation of the experimental conditions for **(a)** starting material synthesis and **(b)** deformation of the bubble-bearing magmas in simple shear (see text for details). **(a)** Sample schematics show the powdered sample before synthesis (1) and after synthesis (2). **(b)** The grey box indicates when deformation occurred, after the sample was brought to equilibrium with the pressure and temperature conditions. In this example, the pore fluid pressures equilibrate across the sample, representing permeability development. Deformation is in right lateral shear. The sample picture is of experiment PP512, after deformation.

Table 1
Experiment list.

Experiment	d (mm)	l (mm)	P_{Ci} (MPa)	P_{Cd} (MPa)	P_u (MPa)	P_d (MPa)	T (°C)	$\dot{\gamma}$ (s^{-1})	γ	η_{app} (Pa s)	k
PP506	14.85	4.44	310	57	22	17	880	s.m.	–	–	No
PP545	16.56	4.63	314	59	26	21	880	9.9×10^{-5}	6.9	1.2×10^{10}	No
PP511	15.12	3.69	320	58	26	21	880	2.2×10^{-4}	7.1	2.0×10^{10}	No
PP512	14.42	3.98	312	58	26	21	880	1.8×10^{-4}	2.9	2.1×10^{10}	unclear
PP509	15.08	4.40	307	58	26	21	880	4.5×10^{-4}	3.4	2.5×10^{10}	Yes
PP444	16.10	4.59	306	57	31	26	880	4.5×10^{-4}	1.6	2.4×10^{10}	No
PP443	15.67	3.55	309	56	33	28	870	5.7×10^{-4}	0.2	–	Yes
PP508	14.81	4.21	307	58	27	22	880	8.1×10^{-4}	0.1	–	Yes
PP439	14.57	7.17	298	56	17	23	880	1.0×10^{-4}	–	–	No
	–	–	–	–	–	–	–	3.0×10^{-4}	–	–	–
	–	–	–	–	–	–	–	6.0×10^{-4}	–	–	–

d and l are the sample diameter and length, respectively, after deformation; P_{Ci} is the confining pressure during starting material synthesis (equal to the pore fluid pressure during synthesis); P_{Cd}, P_u, and P_d are the confining, upstream pore fluid, and downstream pore fluid pressures, respectively, during deformation; T is the temperature at which deformation occurred; $\dot{\gamma}$ is the shear strain rate at the sample periphery (s.m. denotes the starting material and was not deformed); γ is the final strain achieved during the experiment based on sample geometry; η_{app} is the apparent viscosity of the sample at $\gamma = 1$; and k denotes whether permeability was established during the course of deformation.

$10^{7.0}$ Pa s. For a maximum grain size of 90 μm and assuming $\Gamma =$ 0.3 N/m (Bagdassarov et al., 2000), λ_s is approximately 25 min.

After one hour, the sample was isothermally decompressed to 60 MPa at an average rate of 5 MPa/min, while keeping $P_{eff} =$ 0 MPa (Fig. 3A). Decompression allowed bubble expansion, resulting in a two-phase magma containing polydisperse bubbles with a peak and maximum bubble radius of 2 μm and 25 μm, respectively (Fig. 1B). The timescale of relaxation, λ_b, for the bubbles was calculated: $\lambda_b = \frac{a\eta_o}{\Gamma}$, where a is the bubble radius (Mader et al., 2013). For a maximum bubble radius of 25 μm and using a melt viscosity of $10^{7.0}$ Pa s, the relaxation timescale of the bubbles was 14 min. The sample was allowed to equilibrate for 1 h at 1150 °C to ensure that all bubbles attained spherical geometries (Fig. 1C).

Following bubble entrapment and decompression-induced expansion, the sample temperature was decreased to 880 °C at 10 °C/min (see below). The pore fluid pressure was isolated from the confining pressure and the pore fluid pressures upstream (P_u) and downstream (P_d) of the sample were lowered to 25 and 20 MPa, respectively (Fig. 3A). The sample was confirmed to be impermeable if these two pressures did not equilibrate; each sample was then isobarically quenched to room temperature at 43 °C/min. X-ray computed tomography (XCT; Phoenix NanoTOM, ISTO, Orléans, France) confirmed the absence of through-going cooling fractures and that the sample was homogeneously vesicular. All samples were ~15 mm in diameter, between 4 and 7 mm long, had an average total porosity of 0.14 ± 0.01, and a bubble number density of 0.002 μm^{-2} (as determined by image analysis, see below).

2.2. Deformation in simple shear

After synthesis and XCT imaging, straight lines were scribed along the length of the sample assembly jacket to act as passive strain markers, as well as to indicate if any strain was accommodated by slip along the spacer interfaces during deformation.

The viscosity of the melt phase at 1150 °C was too low for deformation to be readily measured in the Paterson apparatus, therefore, we elected to perform all deformation experiments at 880 °C, where the viscosity of anhydrous HPG8 is $\sim 10^{11.0}$ Pa s (Hess et al., 2001). Impermeable samples were put back into the Paterson apparatus, placed under pressure such that $P_c = P_f = 60$ MPa, and heated to 880 °C at 10 °C/min (Fig. 3B). At 880 °C, the confining and pore fluid pressures were isolated from each other and the pore fluid pressure was lowered such that $P_f = 25$ MPa (except in one experiment where $P_f = 40$ MPa, see Supplementary Material; Fig. 3B). P_u and P_d were then isolated from each other and the differential pressure (ΔP) across the sample was set to 5 MPa (Fig. 3B). This served to confirm that the sample was impermeable and the experiment continued under these conditions. We note that because the porosity in all samples was initially unconnected, the pressure in the bubbles was equal to the P_c (i.e. ~60 MPa), thus, the P_{eff} of the sample was 0 MPa as long as the sample remained impermeable.

Samples were deformed in right-lateral simple shear at shear strain rates, $\dot{\gamma}$, between 9.9×10^{-5} and 8.1×10^{-4} s^{-1} (Table 1). Deformation was terminated once samples became permeable (signalled by the equalization of P_u and P_d across the sample; Fig. 3B) or once deformation was in excess of a total bulk shear strain, γ, of ~7. At this viscosity, the relaxation timescale (λ_b) for bubbles with 25 μm radius is 96 days; none of our experiments exceeded 25 h, ensuring that the experiments were performed in the unsteady flow regime (Llewellin et al., 2002). Since samples were isobarically quenched on a timescale $\ll \lambda_b$, we conclude that the deformation microstructures were preserved for microstructural analysis.

During deformation, the centre of the sample experienced zero torque and, therefore, zero strain; both strain and strain rate increased radially toward the sample exterior (Paterson and Olgaard, 2000). The torque applied to the sample was measured using an internal load cell with calibrated linear variable differential transformers (LVDT). Measured torque was corrected for the strength of the iron jacket (Frost and Ashby, 1982) and converted to shear stress: $\tau = M\frac{4(3+\frac{1}{n})}{\pi d^3}$, where M is the torque, d is the diameter of the sample, and n is the stress exponent (Paterson and Olgaard, 2000). n is an unknown empirical parameter that is experimentally determined for a given sample by conducting a strain rate stepping experiment and corresponds to the slope of the log–log plot of radial displacement rate ($\dot{\theta}$) vs. M : $n = \frac{d \ln \dot{\theta}}{d \ln M}$ (Paterson and Olgaard, 2000). Apparent melt viscosity, η_{app}, during deformation was calculated: $\eta_{app}(t) = \frac{\tau(t)}{\dot{\gamma}}$. The relative viscosity, η_{rel}, is given: $\eta_{rel}(t) = \frac{\eta_{app}(t)}{\eta_o}$.

2.3. Microstructural analysis

After deformation, all samples were imaged in 3D in their iron jackets using XCT. To keep the image size manageable for processing, the voxel length was set to 15 μm (voxel volume: 3375 μm^3); this did not provide enough resolution to image bubbles with semi-major axes less than ~15 μm.

After preliminary imaging in the iron jacket, the samples and adjoining permeable spacers (and their encompassing jackets) were cut out of the sample assembly and placed in a solution of 50% nitric acid and 50% hydrochloric acid; this solution dissolved the iron jacket without damaging the sample microstructure. Sam-

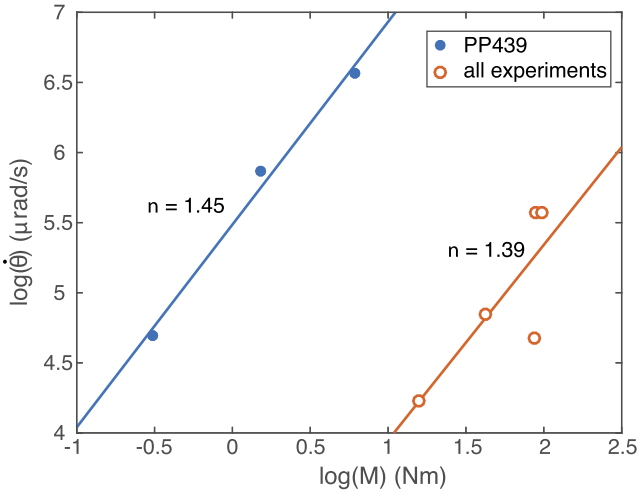

Fig. 4. Log–log plot of radial displacement rate ($\dot{\theta}$) versus torque (M) (corrected for the strength of the iron jacket). Solid, blue dots represent the strain rate stepping experiment, PP439; open, orange dots are the torque of all constant shear strain rate experiments at $\gamma = 1$ and normalized to a standard sample length and diameter, after Champallier et al. (2008).

ples were then placed in epoxy and polished to expose their longitudinal tangential surface, which represents the plane of maximum shear strain (Paterson and Olgaard, 2000).

Microstructural imaging of the samples was carried out using a Mira3 TESCAN scanning electron microscope (SEM; BRGM/Université d'Orléans/ISTO, Orléans, France). The total porosities, 2D bubble geometries, and 2D bubble number densities were determined for the starting material and deformed samples by segmenting SEM images using image-processing software (ImageJ). Bubble geometry was described by the semi-major and semi-minor axes of the best-fit ellipse of each bubble and the angle between the semi-major axis and the spacer interface, θ (Fig. 1).

3. Results

3.1. Mechanical data

We performed seven constant strain rate experiments and one strain rate stepping experiment (Table 1). Using the data provided by the strain rate stepping experiment (PP439), we found a stress exponent, n, of 1.45 (Fig. 4), consistent with shear thinning behaviour (Arbaret et al., 2007). This value is confirmed by the n-value determined using the recorded torque at $\gamma \sim 1$ for all constant shear strain rate experiments performed under the same pressure and temperature conditions and normalized to a standard sample length and diameter, as described by Champallier et al. (2008) (Fig. 4). We emphasize that we chose $\gamma \sim 1$ since all samples exhibited steady state behaviour up to this strain. However, those samples deformed at high shear strain rate experienced an increase in shear stress with increasing shear strain (strain hardening), thus the value of n given here may not adequately describe the data beyond $\gamma \sim 1$. Similarly, we cannot be certain of the non-Newtonian behaviour of the magmas after $\gamma \sim 1$. We note that strain hardening has been observed in simple shear deformation of phonolitic magmas under similar conditions to this study and has been attributed to deformation of the iron jacket (Caricchi et al., 2011); we observed no wrinkling of the iron jacket during our experiments and have no reason to believe that this behaviour is an artefact of our experimental protocol.

The apparent viscosities at $\gamma \sim 1$ for all experiments ranged between 2.5×10^{10} and 1×10^{10} Pa s (Table 1) and the relative viscosities were less than 0.6 for all experiments. A stress–strain plot for all constant strain rate experiments is presented in Fig. 5 and the onset of permeability development is indicated for each experiment (Fig. 5, inset).

Permeability developed in samples deformed at shear strain rates greater than $\sim 2 \times 10^{-4}$ s^{-1} (experiments PP508, PP443, and PP509). At shear strain rates in excess of 4.5×10^{-4} s^{-1} (PP443, PP508), permeability developed immediately after the onset of inelastic deformation (Fig. 5, inset). PP508 experienced four stress drops before the pore fluid pressures equilibrated. We highlight that PP443 was performed at a temperature of 870 °C to ensure that the melt viscosity was such that the glass transition could be crossed, inducing a brittle response in the sample. PP509 ($\dot{\gamma} = 4.5 \times 10^{-4}$ s^{-1}) strain hardened after $\gamma \sim 1$ and permeability developed in the course of strain hardening at $\gamma \sim 3.5$ (Fig. 5, inset); the stress drop at the end of the experiment occurred in conjunction with the equilibration of the pore fluid pressures (see Fig. SM.3 in Supplementary Material). We stress that we did not observe any perturbation in sample temperature with outgassing, as reported by Caricchi et al. (2011). Experiment PP444 ($\dot{\gamma} = 4.5 \times 10^{-4}$ s^{-1}) was terminated at $\gamma \sim 1.6$ to investigate the microstructure of the sample before strain hardening could begin. PP512 ($\dot{\gamma} = 1.8 \times 10^{-4}$ s^{-1}) experienced significant strain hardening but it is unclear from the pore fluid pressure data (see Supplementary Material) if this sample became permeable before the end of the experiment as the jacket ruptured, ending the experiment. Samples deformed at shear strain rates $< 2.2 \times 10^{-4}$ s^{-1} (PP511 and PP545) did not exhibit significant strain hardening nor did they become permeable; these experiments were terminated at $\gamma \sim 7$ (Fig. 5). We note that while PP511 ($\dot{\gamma} = 2.2 \times 10^{-4}$ s^{-1}) exhibited an initial period of strain hardening, the sample strain weakened after $\gamma \sim 1.5$ until the end of the experiment. All pore fluid pressure data can be found in Fig. SM.3 of the Supplementary Material.

3.2. Sample microstructure

In all experiments, bubbles are deformed and their semi-major axes define the dominant sample foliation (see the Supplementary Material for the sample-wide microstructure of the deformed samples). Calculated 2D bubble densities are consistent with the starting material (0.002 μm^{-2}), with the exception of PP509 (0.001 μm^{-2}), and we do not observe microstructure indicative of bubble coalescence.

Five of the deformed samples (PP508, PP443, PP444, PP509, and PP512) contain fractures and all samples that became permeable contain en échelon fracture arrays (Fig. 6). These fractures are situated around the outer circumferences of the samples where shear strains are largest and fracture tips are oriented between 34 and 67° to the shear zone boundaries (Fig. 6). At high strain rate but low strain (e.g. PP443), fractures nucleated at bubble–melt interfaces and in the middle of the melt phase (Fig. 7A). At small strain, these short fractures propagated and interacted (Figs. 7A and B) and appear to have begun to coalesce as the melt bridges between fractures began to thin (Fig. 7B).

At moderate strain rates and large strain (e.g. PP509 and PP512), bubbles intersect and impinge on the fractures (Figs. 7C and D) and the fracture tips are offset along bubble semi-major axes (Fig. 7C), demonstrating that fracture rupture and propagation were concomitant with shear. We do not observe shear displacement of bisected bubbles along the fracture planes (Fig. 7C). In experiment PP509, some fractures became sigmoidal, signalling several fracture generations (Fig. 6) and the most rotated of these fractures are surrounded by zones of bubble-bereft melt (Fig. SM.4D). We also observe that in PP509 the fractures are localized in a band along the sample periphery (Fig. 6). With the exception of PP508 (discussed below), fracture density increases with increasing shear strain rate.

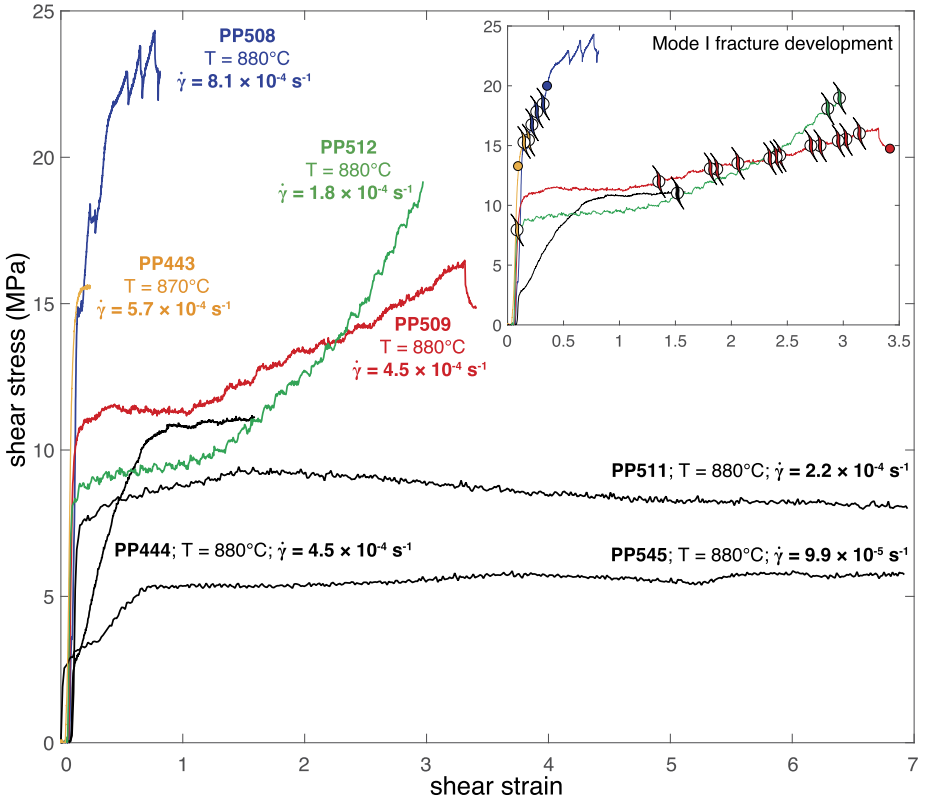

Fig. 5. Mechanical data (shear stress versus shear strain) for all constant shear strain rate experiments. The inset shows the stress versus shear strain data for samples containing Mode I fractures. Sigmoidal symbols denote the strain at which Mode I fractures formed. Coloured circles denote the strain at which the samples became permeable.

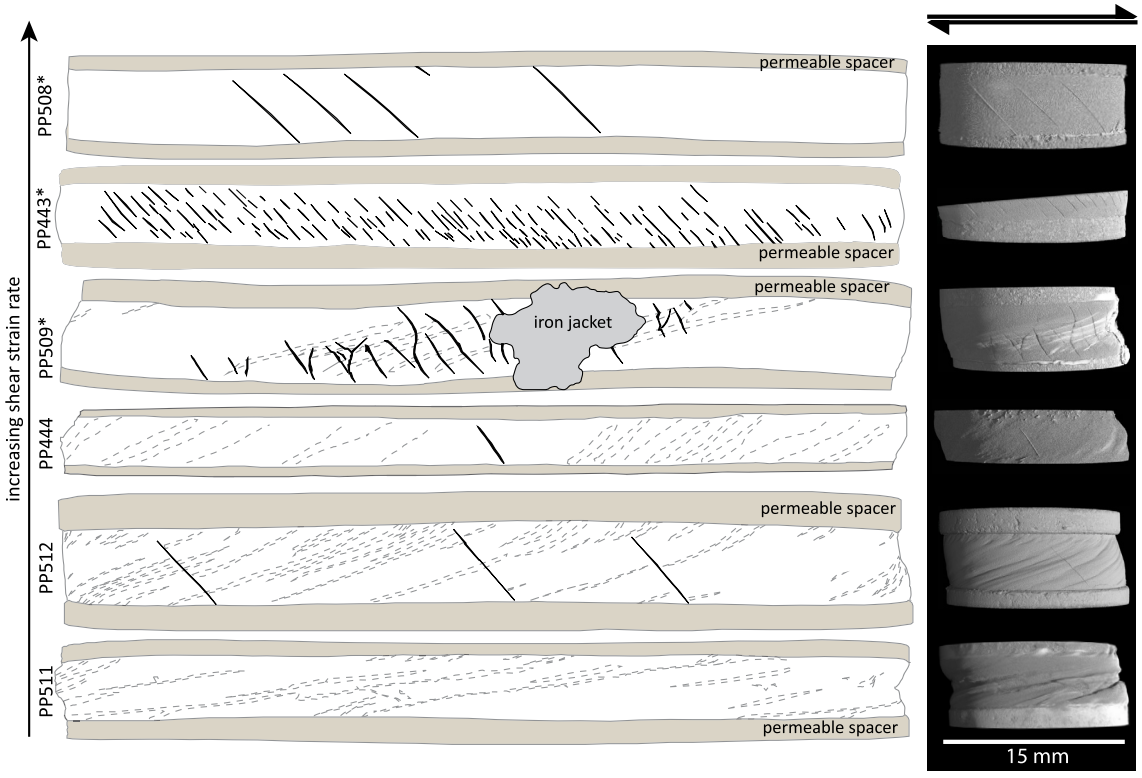

Fig. 6. Structural reconstructions of the sample surfaces from XCT data. XCT surface renderings of the samples are provided in the right-most panel. The dashed lines in the structural drawings represent the overall foliations of the samples. Fractures (solid black) are oriented approximately perpendicular to the dominant foliation. Asterisks indicate samples that became permeable during deformation.

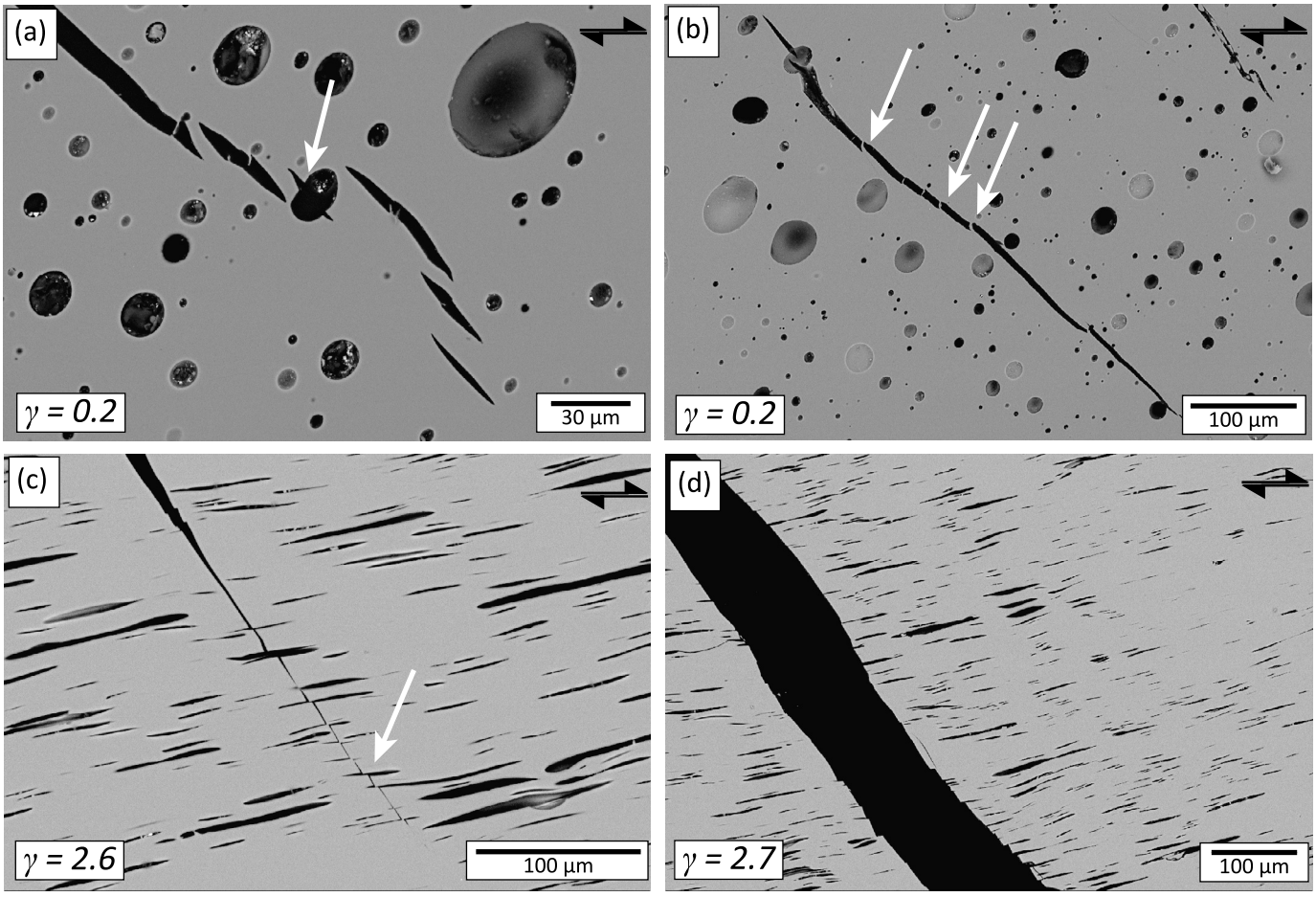

Fig. 7. SEM images of Mode I fractures in deformed products. **(a)** and **(b)** PP443, $\dot{\gamma} = 5.7 \times 10^{-4}$ s^{-1}, $\gamma = 0.2$. **(a)** Mode I fractures nucleate at bubble–melt interfaces (white arrow) and in the melt phase and open in the direction of the least compressive stress, σ_3. **(b)** Adjacent microcracks begin to coalesce as the melt bridges begin to thin and rupture (white arrows). **(c)** PP512, $\dot{\gamma} = 1.8 \times 10^{-4}$ s^{-1}, $\gamma = 2.6$. Fracture tips are offset along bubble major-axes (white arrow); no shear displacement is observed. **(d)** PP509, $\dot{\gamma} = 4.5 \times 10^{-4}$ s^{-1}, $\gamma = 2.7$. Bubbles encroach on fractures, eventually leading to bubble loss in the surrounding melt; see also Supplementary Material. The indicated γ reflect the strain calculated for the imaged plane of the sample.

The microstructure of experiment PP545 could not be accurately determined as the sample broke upon being taken out of the deformation apparatus. Inspection of spacer interfaces showed no slip along the spacer surfaces and the mechanical data were not suspect. The sample remained impermeable during deformation (see Fig. SM.3G of the Supplementary Material).

4. Discussion

4.1. Dominant structural features

4.1.1. Bubbles as passive strain markers

In all samples, the orientation of the semi-major axes of the elongated bubbles defines the global, shear-induced foliation. In steady flow, these orientations record strain, even under the influence of a restoring surface tension force (Rust et al., 2003) and, critically, Arbaret et al. (2007) found that deformed bubbles acted as ideal passive strain markers in haplogranitic melts deformed under similar conditions as the present study. The accumulated strain recorded by a rigid body rotated in simple shear can be calculated: $\gamma = \frac{2}{\tan 2\theta}$ (Ramsay, 1980), where θ is the orientation of the body's semi-major axis with respect to the shear zone boundary. If we assume that bubbles act as proxies for the strain ellipse of the deforming system (that is, they are passively rotating features), then, to a first order, θ is oriented at 45° to the shear zone boundary when deformation commences and approaches 0° with increasing strain (Fig. 8). We compare the weighted mean of the bubble orientations and known bulk strains of the imaged sections for each experiment with the strain predicted by the passive rotation of the strain ellipse (Fig. 8). Despite our experiments having been performed under unsteady flow conditions, the calculated shear strains are in agreement with those predicted for the rotation of a rigid passive strain marker in simple shear (Fig. 8). While the standard deviation in bubble orientations suggests that, locally, strain and strain rate may have varied from the bulk behaviour of the sample, bubble orientations still reflect the total bulk strain expected, even in the presence of fractures (e.g. PP509, Fig. 8). Thus, we conclude that the fractures must have also behaved as passive structures after formation.

4.1.2. The development and evolution of a fracture network

In this study, permeability was established via the formation of fractures. The orientations of the tips of these fractures range between 34 and 67° with respect to the shear zone boundary, similar to those observed experimentally by Okumura et al. (2010). In PP509 and PP512, fracture tips are offset along foliation (Fig. 7C) indicating that they, at some point, propagated synchronously with shear, though we cannot confirm that the fractures propagated continuously after formation. Critically, we observe no displacement of bisected bubbles along the fracture lengths that would suggest shear displacement along these features (Fig. 7C, white arrow). We conclude that the fractures formed in our experiments are neither shear fractures nor Riedel shears but are, instead,

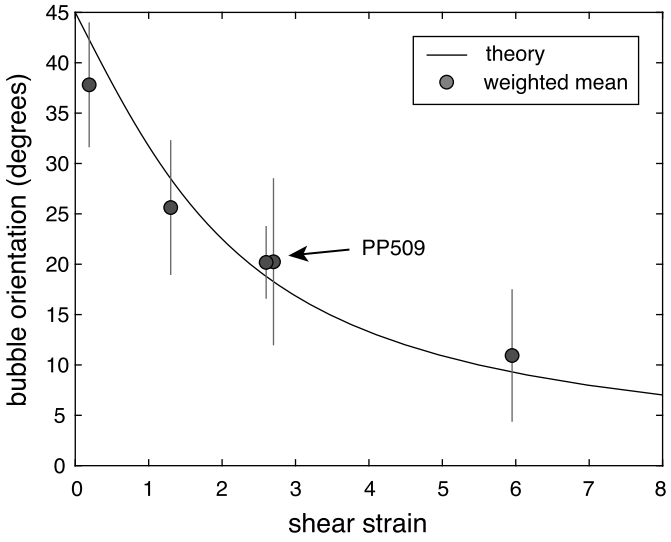

Fig. 8. Bubble orientation for all experiments versus shear strain. The solid black curve represents the orientation of the strain ellipse with increasing shear strain: $\gamma = \frac{2}{\tan 2\theta}$ (Ramsay, 1980). Filled circles are the weighted mean values of bubble orientation for the experiments in this study; vertical lines give orientations within one standard deviation of the mean bubble orientation.

purely extensional (Mode I) features and likely initiated at 45° to the shear zone boundary (Ramsay, 1980). If these features are purely extensional, they opened in the direction of the least compressive stress, σ_3, propagated in the direction of the principal compressive stress, σ_1, and did not accommodate significant strain until they were passively rotated and entrained into the shear direction (Ramsay, 1980).

While we do not consistently observe fracture tip orientations of 45° in all samples, these orientations are common in PP443 (Fig. 6) where fractures developed shortly after deformation commenced. In that sample, we observe two types of fracture nucleation; fractures nucleated either within the melt phase (Fig. 7A) or at pore-melt interfaces (Figs. 7A and B). The latter bear a strong resemblance to pore-emanating fractures, as described by Sammis and Ashby (1986). In that study, spherical voids locally perturbed the stress field such that extension fractures developed during deformation and propagated in the direction of σ_1 and opened in the direction of σ_3. When unconfined ($P_{eff} = 0$), these fractures continued to propagate in σ_1, eventually resulting in sample-wide planes of failure. However, as confining pressure was increased, these fractures began to coalesce at an angle to σ_1 (usually ~30°), resulting in macroscopic failure in shear (Sammis and Ashby, 1986). In our samples, we see no evidence to suggest that the Mode I fractures coalesced to give rise to shear fractures on the timescales of deformation (Fig. 6), though, as a whole, they do appear to have localized in a band in PP509. Our observations are consistent with Mode I fracture development when $P_{eff} = 0$ MPa.

As fractures grew and propagated, dilating and creating more void space, the pore fluid pressure was locally reduced. The pressure gradient between the pores (60 MPa) and the propagating fractures ($\ll$60 MPa) promoted bubble evacuation into the fractures over time (Fig. 7D). In pyroclastic obsidians, fracture development provides low pressure and/or high temperature sites that encourage diffusion of H_2O through the melt phase and into fractures, resulting in gas escape and recorded by dehydrated halos around healed fractures (Cabrera et al., 2011). We emphasize that the pore fluid in our experiments is argon, which has a much lower solubility in silicate melts than H_2O (Carroll and Stolper, 1993). Therefore, while diffusion is the dominant mechanism for H_2O transport toward fractures in natural rhyolites, diffusive mass transport was not likely to have been operative in our system. Volatile migration into fractures in our experiments was a slow and inefficient process and the depletion in bubbles surrounding fractures likely resulted from the evacuation of bubbles intersected by fractures.

The deformed bubbles in PP509 acted as local strain markers, mapping the instantaneous shear strain and shear strain rate between fractures (Fig. SM.4D). These values indicate that shear was localized in the centre of the sample, and petered off towards the spacers. The resultant shear strain rate gradient across the sample gave rise to the sigmoidal shape of the fractures (Lisle, 2013); the sigmoidal fracture geometry resulted from the passive rotation of the centres of the fractures as deformation continued, as opposed to being controlled by the mechanical competence of the bridging melt segments (see Fig. 2 of Lisle, 2013). As such, the strain recorded by the central portion of these fractures can be used to determine when, during deformation, they formed. By comparing the initial and final fracture orientations, we can calculate the strain accumulated during the passive rotation of these features (Ramsay, 1980): $\gamma = \cot\alpha - \cot\alpha'$, where α is the initial orientation of the fracture and α' is the orientation of the fracture after deformation. In our system, we assume $\alpha = 45°$ and α' is the angle formed between the spacer interface and the centres of the sigmoidal fractures. By calculating the strains recorded by these rotated features, we can locate their formation on the stress-strain curves (Fig. 5, inset).

At strain rates higher than 5×10^{-4} s^{-1} (PP508, PP443) fractures formed shortly after deformation began, suggesting that the material was entirely brittle. At strain rates between ~2×10^{-4} and 5×10^{-4} s^{-1} (PP509 and PP512), fracture formation occurred after an initial deformation of at least $\gamma \sim 1$ and was associated with strain hardening. Below $\gamma \sim 1$, samples show little to no strain hardening and there is no evidence of Mode I fracture development. Indeed, the first generation of Mode I fractures in PP509 records a shear strain of $\gamma \sim 2$, placing their formation around $\gamma \sim 1$, where the sample began to exhibit strain hardening. This is reinforced by the single tension gash developed in PP444: it is not sigmoidal, indicating that it was newly formed just prior to the end of that experiment.

4.2. *Fracture-induced mechanical response or experimental artefacts?*

We observed instantaneous drops in stress during deformation in two experiments (i.e. PP508 and PP509; Fig. 5). In torsion, the observation of stress drops during deformation often reflects the development of a sample-scale helical fracture that results in a significant loss of competence of the sample (Rybacki et al., 2010). Further, the observation of oscillatory stress drops during deformation has been interpreted as reflecting fracture and healing cycles in magma (Pistone et al., 2012).

In experiment PP509, the drop in stress (Fig. 5) was associated with the equilibration of pore fluid pressures, confirming that the formation of the Mode I fractures did not significantly alter the mechanical behaviour of the magmas. Indeed, given the orientation of these features and the lack of evidence that they localized shear strain upon formation, we would not expect Mode I fractures to decrease sample competence.

We highlight that the periodic stress drops observed in experiment PP508 were not related to pore pressure equilibration (see Supplementary Material, Fig. SM.3A), sample-wide helical fracture (Fig. 6), or fracture-healing cycles. While the sample did fracture in Mode I and pore fluid equilibration occurred, its material strength was close enough to the friction existent between spacers that slip along these interfaces is likely. Indeed, the strain recorded by the strain markers scribed onto the jacket (Table 1) shows that only a fraction of the predicted strain (Fig. 5) was accommodated by the sample, confirming that strain was partitioned elsewhere in the

system. No slip along spacer interfaces was recorded by the scribed strain markers, leading us to surmise that slip occurred along the upper (or lower) spacer and assembly head interface(s) (see Supplementary Material for a detailed discussion). We conclude that the periodic losses of strength observed during deformation were experimental artefacts related to slip along the interfaces between the spacers and sample assembly head, a consequence of a high shear strain rate that overcame the friction along these surfaces. We, therefore, hazard caution of the interpretation of the mechanical data for PP508.

4.3. The brittle–viscous transition: tearing up magma

While experiment PP443 behaved in a purely brittle manner, experiments PP509 and PP512 typify brittle–ductile shear zones (Ramsay, 1980). Both these samples displayed strain hardening behaviour, which may have been a symptom of local increases in viscosity due to bubble and volatile loss (Schmocker et al., 2003; Shields et al., 2014), as suggested by the decrease in bubble density observed in PP509. In our experiments, older generations of fractures are surrounded by bubble-depleted zones (Fig. SM.4D), which is perhaps a result of differential pressure-induced bubble evacuation into the fractures (see Section 4.1.2). This may have led to a local increase in the bulk viscosity of the magma, resulting in strain hardening. However, in PP512 – which experienced significant strain hardening – we find no evidence of bubble-bereft zones surrounding the fractures. Therefore, aspiration of bubbles into these fractures was not the reason for the observed strain hardening.

In a silicate melt, non-Newtonian viscous flow precedes brittle failure and, ultimately, fracture of silicic magmas occurs when the tensile strength of the magma is exceeded (Webb and Dingwell, 1990a). The relaxation timescale, t_c, for a melt of given viscosity is given by the Maxwell relationship: $t_c = \frac{\eta_0}{G_\infty}$, where G_∞, the unrelaxed elastic shear modulus, is 10^{10} Pa for silicate melts (Webb and Dingwell, 1990b). The onset of non-Newtonian behaviour has been observed to occur at strain rates three orders of magnitude less than the inverse of the structural relaxation time of the liquid (Webb and Dingwell, 1990b). In our system, using a melt viscosity of $10^{11.0}$ Pa s (Hess et al., 2001), the onset of non-Newtonian behaviour should occur at shear strain rates faster than 10^{-4} s^{-1} and brittle failure of the melt phase is expected at strain rates one order of magnitude above this (10^{-3} s^{-1}). While our experiments appear consistent with non-Newtonian shear thinning behaviour below $\gamma \sim 1$ (Fig. 4; see Supplementary Material), this is very likely a result of the presence of highly deformed inviscid bubbles, which increasingly act to limit viscous dissipation in the suspension as bubbles become progressively more deformed (Rust and Manga, 2002).

We posit that the strain hardening of the samples likely reflects the accumulation of stress within the melt and precedes eventual fracture. Indeed, changes in n suggest changes in deformation mechanism (Paterson and Olgaard, 2000) and are consistent with a transition to more brittle behaviour. We note that the degree of strain hardening in PP509 is smaller than in PP512, despite PP509 having been deformed at a faster strain rate. Several generations of tension gash are present in PP509, reflecting multiple excursions across the viscous-brittle transition. Indeed, fracture development began shortly after $\gamma \sim 1$, punctually releasing local build-ups in stresses and globally reducing the strain hardening of the sample. Further, we observe that the Mode I fractures in PP509 form a band across the sample (Fig. 6). This band likely localized shear as the fractures became sigmoidal, muting the strain hardening response of the sample during deformation. Mode I fracture development at strain rates below those predicted for pure melts may indicate strain rate heterogeneities in the sample, or that Mode I fracture development occurs during bubble-induced non-Newtonian flow and dominates in the more ductile end of the brittle-ductile spectrum (Lavallée et al., 2013). If the latter is true, then extension fractures may occur at relatively low strain rates in the conduit and be antecedent to shear fracture development. We emphasize that, at very low strain rates ($<2 \times 10^{-4}$ s^{-1}), the rate of deformation was slow enough that the melt could relax and continue to flow and no Mode I fractures developed; neither fracture nor outgassing occurred under these conditions.

4.4. The efficacy of gas escape

We can qualitatively compare the efficacy of gas egress across our samples (Fig. 9A). In the purely brittle case, PP443, several short fractures were created early during deformation (Figs. 5 and 6). None of these fractures extend across the whole sample and gas flow was dependent on the interconnection of these short, shattered channels. In contrast, in samples where brittle and viscous processes worked in tandem (e.g. PP509 and PP512), fractures are well-developed and extend along the entire length of the sample. Despite taking longer to form, these features are less tortuous and, therefore, more permeable than the fractures formed by purely brittle behaviour (Fig. 9A). Thus, at the onset of percolation, gas egress was most efficient at moderate strain rates ($\sim 4.5 \times 10^{-4}$ s^{-1}; Fig. 9A). We emphasize that the deformation of PP443 was terminated upon gas percolation and, so, integrated over the same deformation timescale as PP509 (that is, to $\gamma \sim 3.5$), the permeability of PP443 would be expected to be very high owing to the continued brecciation of the sample during deformation. However, given the relative scale of these fractures, such a brecciated zone likely would not extend far into a volcanic conduit, limiting the region outgassed by these features.

5. Opening a closed system: implications for the explosive–effusive transition of volcanic eruptions

Mode I fractures are not a rarity in volcanic systems. Indeed, occurrences of Mode I fractures, so called tension gashes, have been documented at trachybasaltic volcanic dyke margins (Petronis et al., 2013) and in obsidian flows (Shields et al., 2016). En échelon, elongate, fissure-like pores have also been interpreted as extension features reflecting the transition from viscous to brittle deformation in extruding dacitic lava domes (Smith et al., 2001). Significantly, variably-healed and ash-filled shear and extension fractures have been identified in rhyolitic systems at exposed conduit margins (Stasiuk et al., 1996; Tuffen and Dingwell, 2005) and in ballistic bombs (Castro et al., 2012), suggesting that fracture processes are common in the upper conduit. Indeed, our experiments demonstrate that these processes can occur under conditions appropriate for effusion in the upper conduit where melt viscosities are high (Goto, 1999) and shear strain rates range between 10^{-2} and 10^{-6} s^{-1} (Tuffen et al., 2003).

Depending on the initial water content of a rhyolitic melt phase in nature, the bubble fraction used in this study may correspond to anywhere above 3500 m depth, for H_2O contents less than 5 wt.% (Okumura et al., 2009 and references therein). Consider, for instance, two rhyolitic eruptions that show evidence of syn-eruptive magma fracture: the 19–21 Ma eruption at Mule Creek (New Mexico, USA; Stasiuk et al., 1996) and the 2008 eruption of volcán Chaitén (Chile; Castro and Dingwell, 2009). In those systems, we estimate that the magmas had bubble fractions of ~0.14 at depths of 1200 m and 2400 m at Mule Creek and

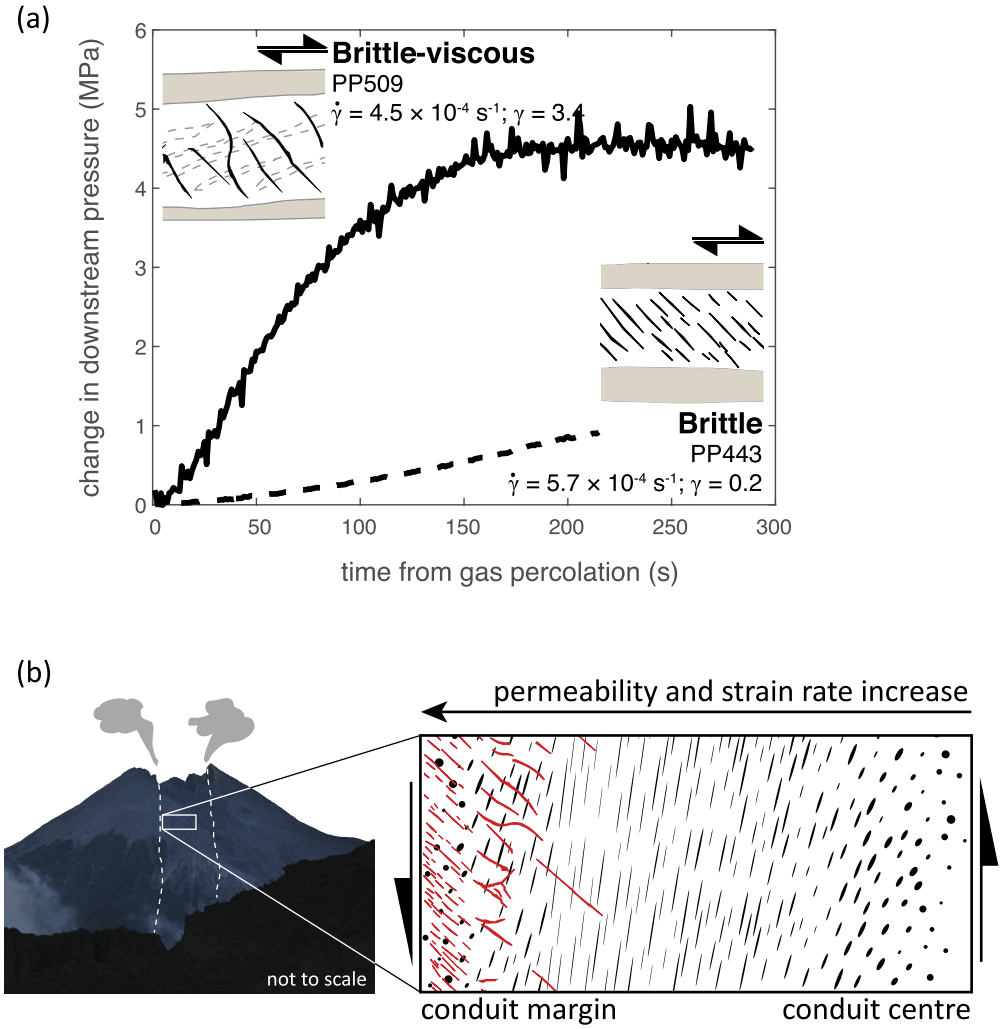

Fig. 9. **(a)** Downstream pore fluid pressure (P_d) equilibration upon permeability development for PP509 and PP443. The inset images are the fracture geometries for the two experiments. **(b)** Schematic of the fracture network near conduit margins. Mode I (extension) fractures propagate upward from the conduit centre and out toward the conduit margins. At percolation (the initial development of permeability), gas egress is most efficient away from the conduit edge, owing to well-developed, large fractures. Despite high fracture densities near conduit margins, gas flow is retarded by the tortuous interconnections of small fractures.

Chaitén, respectively [we estimated H_2O saturation pressures using VolatileCalc (Newman and Lowenstern, 2002) and the pre-eruptive water contents and magma temperatures from Stasiuk et al. (1996) and Castro and Dingwell (2009); vesicularity was estimated following Jaupart and Tait (1990) and we calculated depths assuming lithostatic pressure]. These estimates assume equilibrium dehydration and closed system degassing, which may not be an appropriate model when gas can be siphoned out of the magma along conduit margins and into the surrounding country rock (Stasiuk et al., 1996). Thus, these calculations likely overestimate the vesicularities of these systems at any given depth. It is therefore reasonable that the fracture mechanisms highlighted in this study are operative within the upper conduit, though we stress that several outgassing mechanisms are likely active concurrently. While bubble coalescence may dominate at high bubble fractions, as gas continues to be lost from the system, magma fracture will become increasingly important, further facilitating gas escape.

In the upper conduit, shear-induced fractures at conduit margins form efficient outgassing pathways (Goto, 1999; Gonnermann and Manga, 2003) but, since shear fractures are prone to closure as they accommodate strain (Okumura et al., 2010) or heal (Tuffen and Dingwell, 2005), repeated fracture events may be needed to maintain permeability. Critically, the application of a constant shear strain rate in our experiments appears to keep low-pressure extension zones open up to high strain (e.g. PP509). The passive nature of the Mode I fractures in the present study suggests that they remain ideal, and long-lived, outgassing channels until they are rotated into the shearing direction. Furthermore, we demonstrate that repeated fracture events occur under continuous shear, maintaining the permeable network as deformation continues (as demonstrated in PP509).

Finally, while fracture density is largest at the conduit margins because of locally high strain rates (Lavallée et al., 2013), outgassing through shear fractures may be inefficient since these features are not ideally oriented to facilitate outgassing of the conduit centre (Okumura et al., 2010; Castro et al., 2012). In our experiments, we find no microstructural evidence of shear fractures (though the Mode I fractures may eventually become rotated into the shear direction and, belatedly, localize strain). Instead, Mode I fractures, like Riedel shears (Laumonier et al., 2011), provide ideally oriented outgassing paths from more central regions of the conduit to the conduit margins (Fig. 9B). Therefore, shear-induced fracture geometries do not exclude outgassing of the centre of the magma column and may play a critical role in diffusing gas overpressures in that region of the conduit.

6. Conclusions

The deformation mechanisms associated with permeability development in magma have a profound influence on the longevity and geometry of these outgassing networks. We highlight the importance of Mode I (extension) fractures as passive and relatively long-lived features that assist outgassing at conduit margins. In our experiments, Mode I fractures form efficient outgassing networks, at once creating low-tortuosity pathways across sample lengths and low-pressure void spaces that may siphon surrounding volatiles out of the magma. These fractures localize little strain and, therefore, have a limited effect on the mechanical behaviour of the material until they are rotated into the direction of shear, at which point, they may begin to induce a strain weakening response. At high strain rates and low shear strain, in particular, fracture density is high but fractures are short and gas escape is inefficient, relying on the interconnection of thin fractures to deliver gas across the system. While at lower strain rates fractures take longer to develop, they extend across the whole sample, creating efficient networks for gas escape. Repeated fracture events and relatively low strain localization ensure that these fracture networks encourage sustained outgassing. Critically, when applied to a volcanic setting, the fracture network geometry creates fluid flow pathways that extend from the centre of the volcanic conduit, directing gas upward and outward toward the conduit rim, modulating gas escape and favouring magma effusion.

Acknowledgements

We would like to extend our sincere thanks to T. Mather for her editorial handling of the manuscript and F. Wadsworth and an anonymous reviewer for their insightful comments, which greatly improved the article. We would also like to thank A. Rust, Y. Lavallée, M. Violay, J.-L. Bourdier, J. Castro, J. Farquharson, J.K. Russell, and M.J. Heap for helpful discussions. Funding for research costs was provided by the Agence Nationale de la Recherche (ANR) project DOMERAPI (ANR-12-BS06-0012). Additional funding for ARLK was provided by a Postgraduate Scholarship-Doctoral (CGSD3-444207-2013) provided by the Natural Sciences and Engineering Research Council of Canada (NSERC). I. Di Carlo is thanked for SEM assistance. S. Janiec and P. Benoist are acknowledged for thin section preparation. We thank Q. Thibault for his dedicated guardianship of the Paterson apparatus.

Appendix A. Supplementary material

Supplementary material related to this article can be found online at http://dx.doi.org/10.1016/j.epsl.2016.10.053.

References

Arbaret, L., Bystricky, M., Champallier, R., 2007. Microstructures and rheology of hydrous synthetic magmatic suspensions deformed in torsion at high pressure. J. Geophys. Res., Solid Earth 112 (B10). http://dx.doi.org/10.1029/2006jb004856.

Bagdassarov, N., Dorfman, A., Dingwell, D.B., 2000. Effect of alkalis, phosphorus, and water on the surface tension of haplogranite melt. Am. Mineral. 85 (1), 33–40.

Burgisser, A., Gardner, J.E., 2004. Experimental constraints on degassing and permeability in volcanic conduit flow. Bull. Volcanol. 67 (1), 42–56. http://dx.doi.org/10.1007/s00445-004-0359-5.

Cabrera, A., Weinberg, R.F., Wright, H.M.N., Zlotnik, S., Cas, R.A.F., 2011. Melt fracturing and healing: a mechanism for degassing and origin of silicic obsidian. Geology 39 (1), 67–70. http://dx.doi.org/10.1130/g31355.1.

Caricchi, L., Pommier, A., Pistone, M., Castro, J., Burgisser, A., Perugini, D., 2011. Strain-induced magma degassing: insights from simple-shear experiments on bubble bearing melts. Bull. Volcanol. 73 (9), 1245–1257. http://dx.doi.org/10.1007/s00445-011-0471-2.

Carroll, M.R., Stolper, E.M., 1993. Noble-gas solubilities in silicate melts and glasses – new experimental results for argon and the relationship between solubility and ionic porosity. Geochim. Cosmochim. Acta 57 (23–24), 5039–5051. http://dx.doi.org/10.1016/0016-7037(93)90606-w.

Castro, J.M., Cordonnier, B., Tuffen, H., Tobin, M.J., Puskar, L., Martin, M.C., Bechtel, H.A., 2012. The role of melt-fracture degassing in defusing explosive rhyolite eruptions at volcan Chaiten. Earth Planet. Sci. Lett. 333, 63–69. http://dx.doi.org/10.1016/j.epsl.2012.04.024.

Castro, J.M., Dingwell, D.B., 2009. Rapid ascent of rhyolitic magma at Chaiten volcano, Chile. Nature 461 (7265), 780-U729. http://dx.doi.org/10.1038/nature08458.

Champallier, R., Bystricky, M., Arbaret, L., 2008. Experimental investigation of magma rheology at 300 MPa: from pure hydrous melt to 76 vol.% of crystals. Earth Planet. Sci. Lett. 267 (3–4), 571–583. http://dx.doi.org/10.1016/j.epsl.2007.11.065.

Cordonnier, B., Caricchi, L., Pistone, M., Castro, J., Hess, K.U., Gottschaller, S., Manga, M., Dingwell, D.B., Burlini, L., 2012. The viscous–brittle transition of crystal-bearing silicic melt: direct observation of magma rupture and healing. Geology 40 (7), 611–614. http://dx.doi.org/10.1130/g3914.1.

Eichelberger, J.C., Carrigan, C.R., Westrich, H.R., Price, R.H., 1986. Non-explosive silicic volcanism. Nature 323, 598–602.

Frost, H.J., Ashby, M.F., 1982. Deformation-Mechanism Maps: The Pasticity and Creep of Metals and Ceramics. Pergamon Press.

Gaunt, H.E., Sammonds, P.R., Meredith, P.G., Smith, R., Pallister, J.S., 2014. Pathways for degassing during the lava dome eruption of Mount St. Helens 2004–2008. Geology 42 (11), 947–950. http://dx.doi.org/10.1130/g35940.1.

Gonnermann, H.M., Manga, M., 2003. Explosive volcanism may not be an inevitable consequence of magma fragmentation. Nature 426 (6965), 432–435. http://dx.doi.org/10.1038/nature02138.

Goto, A., 1999. A new model for volcanic earthquake at Unzen Volcano: melt rupture model. Geophys. Res. Lett. 26 (16), 2541–2544. http://dx.doi.org/10.1029/1999gl900569.

Hess, K.U., Dingwell, D.B., Gennaro, C., Mincione, V., 2001. Viscosity-temperature behaviour of dry melts in the Qz–Ab–Or system. Chem. Geol. 174 (1–3), 133–142. http://dx.doi.org/10.1016/s0009-2541(00)00312-0.

Holtz, F., Behrens, H., Dingwell, D.B., Taylor, R.P., 1992. Water solubility in aluminosilicate melts of haplogranite composition at 2 kbar. Chem. Geol. 96 (3–4), 289–302. http://dx.doi.org/10.1016/0009-2541(92)90060-i.

Jaupart, C., Tait, S., 1990. Dynamics of eruptive phenomena. Rev. Miner. 24, 213–238.

Kennedy, B., Spieler, O., Scheu, B., Kueppers, U., Taddeucci, J., Dingwell, D.B., 2005. Conduit implosion during vulcanian eruptions. Geology 33 (7), 581–584. http://dx.doi.org/10.1130/g21488.1.

Laumonier, M., Arbaret, L., Burgisser, A., Champallier, R., 2011. Porosity redistribution enhanced by strain localization in crystal-rich magmas. Geology 39 (8), 715–718. http://dx.doi.org/10.1130/g31803.1.

Lavallée, Y., Benson, P.M., Heap, M.J., Hess, K.U., Flaws, A., Schillinger, B., Meredith, P.G., Dingwell, D.B., 2013. Reconstructing magma failure and the degassing network of dome-building eruptions. Geology 41 (4), 515–518. http://dx.doi.org/10.1130/g33948.1.

Lavallée, Y., et al., 2015. Thermal vesiculation during volcanic eruptions. Nature 528 (7583), 544. http://dx.doi.org/10.1038/nature16153.

Lisle, R.J., 2013. Shear zone deformation determined from sigmoidal tension gashes. J. Struct. Geol. 50, 35–43. http://dx.doi.org/10.1016/j.jsg.2012.08.002.

Llewellin, E.W., Mader, H.M., Wilson, S.D.R., 2002. The rheology of a bubbly liquid. Proc. R. Soc. A, Math. Phys. Eng. Sci. 458 (2020), 987–1016. http://dx.doi.org/10.1098/rspa.2001.0924.

Mader, H.M., Llewellin, E.W., Mueller, S.P., 2013. The rheology of two-phase magmas: a review and analysis. J. Volcanol. Geotherm. Res. 257, 135–158. http://dx.doi.org/10.1016/j.jvolgeores.2013.02.014.

Martel, C., Iacono-Marziano, G., 2015. Timescales of bubble coalescence, outgassing, and foam collapse in decompressed rhyolitic melts. Earth Planet. Sci. Lett. 412, 173–185. http://dx.doi.org/10.1016/j.epsl.2014.12.010.

Newman, S., Lowenstern, J.B., 2002. VOLATILECALC: a silicate melt–H_2O–CO_2 solution model written in Visual Basic for Excel. Comput. Geosci. 28 (5), 597–604. http://dx.doi.org/10.1016/s0098-3004(01)00081-4.

Okumura, S., Nakamura, M., Nakano, T., Uesugi, K., Tsuchiyama, A., 2010. Shear deformation experiments on vesicular rhyolite: implications for brittle fracturing, degassing, and compaction of magmas in volcanic conduits. J. Geophys. Res., Solid Earth 115. http://dx.doi.org/10.1029/2009jb006904.

Okumura, S., Nakamura, M., Takeuchi, S., Tsuchiyama, A., Nakano, T., Uesugi, K., 2009. Magma deformation may induce non-explosive volcanism via degassing through bubble networks. Earth Planet. Sci. Lett. 281 (3–4), 267–274. http://dx.doi.org/10.1016/j.epsl.2009.02.036.

Okumura, S., Nakamura, M., Tsuchiyama, A., Nakano, T., Uesugi, K., 2008. Evolution of bubble microstructure in sheared rhyolite: formation of a channel-like bubble network. J. Geophys. Res., Solid Earth 113 (B7). http://dx.doi.org/10.1029/2007jb005362.

Paterson, M.S., Olgaard, D.L., 2000. Rock deformation tests to large shear strains in torsion. J. Struct. Geol. 22, 1341–1358.

Petronis, M.S., Delcamp, A., de Vries, B.v.W., 2013. Magma emplacement into the Lemptegy scoria cone (Chaine Des Puys, France) explored with structural, anisotropy of magnetic susceptibility, and Paleomagnetic data. Bull. Volcanol. 75 (10). http://dx.doi.org/10.1007/s00445-013-0753-y.

Pistone, M., Caricchi, L., Ulmer, P., Burlini, L., Ardia, P., Reusser, E., Marone, F., Arbaret, L., 2012. Deformation experiments of bubble- and crystal-bearing magmas: rheological and microstructural analysis. J. Geophys. Res., Solid Earth 117. http://dx.doi.org/10.1029/2011jb008986.

Ramsay, J.G., 1980. Shear zone geometry – a review. J. Struct. Geol. 2 (1–2), 83–99. http://dx.doi.org/10.1016/0191-8141(80)90038-3.

Rust, A.C., Cashman, K.V., 2004. Permeability of vesicular silicic magma: inertial and hysteresis effects. Earth Planet. Sci. Lett. 228, 93–107. http://dx.doi.org/10.1016/j.epsl.2004.09.025.

Rust, A.C., Manga, M., 2002. Effects of bubble deformation on the viscosity of dilute suspensions. J. Non-Newton. Fluid Mech. 104 (1), 53–63. http://dx.doi.org/10.1016/s0377-0257(02)00013-7.

Rust, A.C., Manga, M., Cashman, K.V., 2003. Determining flow type, shear rate and shear stress in magmas from bubble shapes and orientations. J. Volcanol. Geotherm. Res. 122 (1–2), 111–132. http://dx.doi.org/10.1016/s0377-0273(02)00487-0.

Rybacki, E., Wirth, R., Dresen, G., 2010. Superplasticity and ductile fracture of synthetic feldspar deformed to large strain. J. Geophys. Res., Solid Earth 115. http://dx.doi.org/10.1029/2009jb007203.

Sammis, C.G., Ashby, M.F., 1986. The failure of brittle porous solids under compressive stress states. Acta Metall. 34 (3), 511–526. http://dx.doi.org/10.1016/0001-6160(86)90087-8.

Schmocker, M., Bystricky, M., Kunze, K., Burlini, L., Stunitz, H., Burg, J.P., 2003. Granular flow and Riedel band formation in water-rich quartz aggregates experimentally deformed in torsion. J. Geophys. Res., Solid Earth 108 (B5). http://dx.doi.org/10.1029/2002jb001958.

Shields, J.K., Mader, H.M., Caricchi, L., Tuffen, H., Mueller, S., Pistone, M., Baumgartner, L., 2016. Unravelling textural heterogeneity in obsidian: shear-induced outgassing in the Rocche Rosse flow. J. Volcanol. Geotherm. Res. 310, 137–158. http://dx.doi.org/10.1016/j.jvolgeores.2015.12.003.

Shields, J.K., Mader, H.M., Pistone, M., Caricchi, L., Floess, D., Putlitz, B., 2014. Strain-induced outgassing of three-phase magmas during simple shear. J. Geophys. Res., Solid Earth 119 (9), 6936–6957. http://dx.doi.org/10.1002/2014jb011111.

Smith, J.V., Miyake, Y., Oikawa, T., 2001. Interpretation of porosity in dacite lava domes as ductile–brittle failure textures. J. Volcanol. Geotherm. Res. 112 (1–4), 25–35. http://dx.doi.org/10.1016/s0377-0273(01)00232-3.

Sparks, R.S.J., 1978. The dynamics of bubble formation and growth in magmas: a review and analysis. J. Volcanol. Geotherm. Res. 3, 1–37.

Stasiuk, M.V., Barclay, J., Carroll, M.R., Jaupart, C., Ratte, J.C., Sparks, R.S.J., Tait, S.R., 1996. Degassing during magma ascent in the Mule Creek vent (USA). Bull. Volcanol. 58 (2–3), 117–130. http://dx.doi.org/10.1007/s004450050130.

Thomas, M.E., Neuberg, J., 2012. What makes a volcano tick – a first explanation of deep multiple seismic sources in ascending magma. Geology 40 (4), 351–354. http://dx.doi.org/10.1130/g32868.1.

Tuffen, H., Dingwell, D., 2005. Fault textures in volcanic conduits: evidence for seismic trigger mechanisms during silicic eruptions. Bull. Volcanol. 67 (4), 370–387. http://dx.doi.org/10.1007/s00445-004-0383-5.

Tuffen, H., Dingwell, D.B., Pinkerton, H., 2003. Repeated fracture and healing of silicic magma generate flow banding and earthquakes? Geology 31 (12), 1089–1092. http://dx.doi.org/10.1130/g19777.1.

Wadsworth, F.B., Vasseur, J., von Aulock, F.W., Hess, K.-U., Scheu, B., Lavallée, Y., Dingwell, D.B., 2014. Nonisothermal viscous sintering of volcanic ash. J. Geophys. Res., Solid Earth 119 (12), 8792–8804. http://dx.doi.org/10.1002/2014jb011453.

Webb, S.L., Dingwell, D.B., 1990a. Non-Newtonian rheology of igneous melts at high stresses and strain rates – experimental results for rhyolite, andesite, basalt, and nephelinite. J. Geophys. Res., Solid Earth Planets 95 (B10), 15695–15701. http://dx.doi.org/10.1029/JB095iB10p15695.

Webb, S.L., Dingwell, D.B., 1990b. The onset of non-Newtonian rheology of silicate melts – a fiber elongation study. Phys. Chem. Miner. 17 (2), 125–132.

Woods, A.W., Koyaguchi, T., 1994. Transitions between explosive and effusive eruptions of silicic magmas. Nature 370 (6491), 641–644. http://dx.doi.org/10.1038/370641a0.